

RESEARCH ARTICLE

Wake analysis of aerodynamic components for the glide envelope of a jackdaw (*Corvus monedula*)

Marco KleinHeerenbrink*, Kajsa Warfvinge and Anders Hedenström*

ABSTRACT

Gliding flight is a relatively inexpensive mode of flight used by many larger bird species, where potential energy is used to cover the cost of aerodynamic drag. Birds have great flexibility in their flight configuration, allowing them to control their flight speed and glide angle. However, relatively little is known about how this flexibility affects aerodynamic drag. We measured the wake of a jackdaw (*Corvus monedula*) gliding in a wind tunnel, and computed the components of aerodynamic drag from the wake. We found that induced drag was mainly affected by wingspan, but also that the use of the tail has a negative influence on span efficiency. Contrary to previous work, we found no support for the separated primaries being used in controlling the induced drag. Profile drag was of similar magnitude to that reported in other studies, and our results suggest that profile drag is affected by variation in wing shape. For a folded tail, the body drag coefficient had a value of 0.2, rising to above 0.4 with the tail fully spread, which we conclude is due to tail profile drag.

KEY WORDS: Gliding flight, Biomechanics, Aerodynamics, Wing morphology, Particle image velocimetry, PIV, Wind tunnel

INTRODUCTION

Gliding flight in birds is a relatively inexpensive mode of flying, at least in terms of instantaneous power required from the flight muscles (Baudinette and Schmidt-Nielsen, 1974). A bird only has to spend energy on keeping the wings spread. The cost of transport is covered by converting potential energy (altitude) into aerodynamic work. During soaring, potential energy is replenished by extracting energy from the environment, for example, from the rising air in thermals (thermal soaring) or the wind shear gradient over the oceans (dynamic soaring). In the absence of external energy sources, a bird will need to use muscle power to gain altitude. Either way, gliding birds have a good reason to minimize aerodynamic drag. However, one can also think of circumstances in which it is beneficial to rapidly dissipate energy, for example, during descent before landing. To accomplish this, birds can modify their flight configuration. The glide performance of birds has been studied in numerous previous works using tiltable wind tunnels (Henningsson and Hedenström, 2011; Pennycuick, 1968; Rosén and Hedenström, 2001; Tucker, 1987; Tucker and Heine, 1990; Tucker and Parrott, 1970) or using field observations (Eder et al., 2015; Pennycuick, 1971). However, it has always been difficult to measure the different

components of drag. One strategy has been to mount body parts on a balance (Lentink et al., 2007; Pennycuick, 1968; Pennycuick et al., 1988; Tucker, 1990); however, it is not trivial to match the degree of flexibility in posture of a bird. There have been few attempts with wake pressure surveys behind the wings of living birds (Pennycuick et al., 1992), but this method only samples a small part of the wing at the time. As a result of advances in technology, we can now measure the entire wake of a bird in one instance, compute the different components of drag and relate them to adjustments in the bird's flight configuration.

In steady gliding flight, the weight (W) of the bird is balanced by the aerodynamic force (Fig. 1A). By definition, this force is decomposed into a lift component L perpendicular to the flight path:

$$L = W \cos \gamma, \quad (1)$$

and a drag component D in the direction along the flight path:

$$D = W \sin \gamma, \quad (2)$$

where γ is the angle between the flight path and the horizontal plane (see Fig. 1B). Using a tiltable wind tunnel (Pennycuick, 1968; Rosén and Hedenström, 2001) or by measuring the glide path (in relation to wind currents) in wild birds (Eder et al., 2015; Pennycuick, 1971), these equations can be used to determine the total drag experienced by a bird. Drag can be decomposed into three main sources. Lift-induced drag (D_{ind}) is the cost of producing lift using wings. From the theory of flight mechanics, we know this component behaves as:


$$D_{\text{ind}} = \frac{L^2}{q\pi eb_w^2}, \quad (3)$$

where L is the lift force; $q = \frac{1}{2}\rho U^2$ is the dynamic pressure, itself a function of density ρ and airspeed U ; b_w is the wingspan; and e is the span efficiency factor (alternatively found in literature as its reciprocal $k_{\text{ind}} = 1/e$). The latter factor is an indicator of how efficiently lift is produced compared with an elliptically loaded planar wing of span b . From Eqn 3 it can be expected that a bird can increase induced drag by flexing its wings. We will refer to the inflight wingspan as b'_w and the related span efficiency as $e' = e/\beta^2$, using $\beta = b'_w/b_w$ as the ratio between inflight span and maximum span. The shape-specific span efficiency e' depends on the load distribution along the span of the wing, where $e' = 1$ is the reference of an elliptically loaded planar wing. This factor can be influenced by non-planar features, e.g. spanwise camber (Cone, 1962), vertical separation of the outer primaries (Tucker, 1993) and, in the case of a loaded tail, the vertical gap between the tail and the main wing (Thomas, 1996).

Another component of drag is the wing profile drag, which describes more local interaction between the airflow and the wing

Department of Biology, Lund University, Lund SE-223 62, Sweden.

*Authors for correspondence (Marco.Klein_Heerenbrink@biol.lu.se; Anders.Hedenstrom@biol.lu.se)

 M.K., 0000-0001-8172-8121; K.W., 0000-0003-1038-8953; A.H., 0000-0002-1757-0945

Received 3 December 2015; Accepted 2 March 2016

List of symbols

b_w	maximum wingspan
$b'_{L>}$	in-flight span of wings (b'_w) or tail (b'_t)
C_D	drag coefficient
C'_D	drag coefficient for specific in-flight wing area
C_L	lift coefficient
C'_L	lift coefficient for specific in-flight wing area
D	drag force
e	span efficiency
e'	span efficiency for specific in-flight wingspan
L	lift force
q	dynamic pressure
Re	Reynolds number
S_b	body frontal area
S_t	tail area
S_w	maximum wing area
S'_w	in-flight wing area
\mathbf{u}	wake velocity vector field with components u , v and w in the x , y and z directions, respectively
U_∞	free-stream speed
W	weight of the bird
β	span ratio with maximum wingspan
γ	glide angle
ζ	area ratio
η_p	vertical separation of primary 8 normalized to in-flight span
η_t	vertical tail gap normalized to in-flight span
η_w	spanwise camber normalized to in-flight span
ρ	density
ψ	stream function
ω	streamwise component of the vorticity field

surface. This component is commonly expressed as:

$$D_{\text{pro}} = q C_{D_{\text{pro}}} S_w, \quad (4)$$

where S_w is the wing area and $C_{D_{\text{pro}}}$ is the profile drag coefficient. Eqn 4 suggests that birds can reduce this component of drag by flexing their wings, which, combined with the span dependency of

induced drag, leads to an optimal span model (Tucker, 1987). With $\zeta = S'_w/S_w$, the coefficient $C'_{D_{\text{pro}}} = C_{D_{\text{pro}}}/\zeta$ represents the shape-specific profile drag coefficient, which may vary because of pressure distribution and the state of the boundary layer across the exposed area of the shape. For a typical aerofoil, the profile drag coefficient varies with the lift coefficient following:

$$C'_{D_{\text{pro}}} = C_{D_0} + k_{\text{pro}}(C'_L - C'_{L_{D_{\text{pro,min}}}})^2, \quad (5)$$

or $C'_{D_{\text{pro}}} = c_0 + c_1 C'_L + c_2 C'^2_L$, where $C'_L = L/qS'_w$ is the shape-specific lift coefficient (Tucker, 1987).

The last component is the body drag, which describes the local interaction between the airflow and the body (and appendages). This component can be expressed as:

$$D_{\text{body}} = q C_{D_b} S_b, \quad (6)$$

where the reference area is now the body frontal area S_b , and the body drag coefficient C_{D_b} describes the characteristics of the body shape. For body frontal area, we use the allometric relationship $S_b = 0.0129 m^{0.614} = 5.0 \times 10^{-3} \text{ m}^2$ (where m is body mass) from Hedenström and Rosén (2003), which corresponds to a disc radius of approximately 4 cm. The body drag coefficient may vary with Reynolds number, $Re = Ul/v$, where l is a characteristic length and v is the kinematic viscosity of air (Hedenström and Liechti, 2001), body angle (Hoerner, 1965), extension of the legs (Pennycuick, 1968) and tail deployment (Thomas, 1996).

With the emergence of particle image velocimetry (PIV) it is now possible to measure the flow field in the wake behind a flying bird (Spedding et al., 2003). This wake contains information about the forces that the bird applied to the air as it passed through it (Henningsson and Hedenström, 2011; Pennycuick et al., 1992; Spedding, 1987). With the current state of technology we can differentiate between the different drag sources in a freely gliding bird, measuring profile drag and body drag as the streamwise velocity deficit and induced drag as the cross-flow kinetic energy. We can then relate the variation in these forces with the variation in posture, and hence work out how birds control their flight. In this paper we present such measurements from the wake of a jackdaw [*Corvus monedula* (Linnaeus 1758)] gliding in a tiltable wind tunnel. We investigate the hypotheses that: (1) span efficiency increases with spanwise camber, primary separation and by use of the tail; (2) profile drag coefficient is controlled by wing shape; and (3) body drag coefficient is increased by body angle and the use of the tail.

MATERIALS AND METHODS

The methods used in the experiments are largely similar to those described in Rosén and Hedenström (2001), with the addition of a Trefftz-plane flow velocity measurement using a stereo PIV system and a stereo camera setup for three-dimensional reconstruction of posture.

Experimental setup

For the experiments, we used the low-turbulence tiltable wind tunnel at the Department of Biology, Lund University, Sweden. Details of the tunnel are described in Pennycuick et al. (1997). The test section is 1.20 m wide, 1.08 m high, and the closed section is approximately 1.2 m long. Downstream of this section is an approximately 0.5-m-long gap that allows easy access to the bird and provides room for positioning PIV cameras outside of the flow (Fig. 1B).

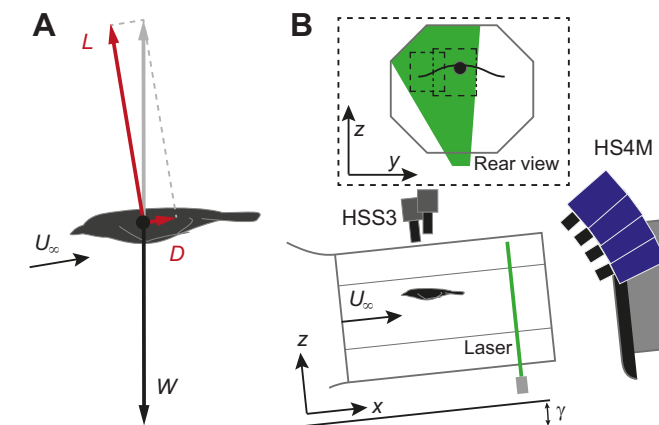


Fig. 1. Schematic representation of the wind tunnel setup for measuring glide performance. (A) Force balance on a bird in steady glide. The vector sum of lift L and drag D balance the weight W . U_∞ is the free-stream speed. (B) The wind tunnel is tilted to a glide angle $\gamma = \{4.5, 5.0, 5.5, 6.0 \text{ deg}\}$. Two high-speed cameras (HSS3) record the posture of the gliding bird. Four high-speed cameras (HS4M) record the movement of suspended oil droplets, which are illuminated by a laser sheet (laser). The inset (rear view) shows the two fields of view of the double stereo PIV configuration: one capturing the wake from the wing tip and the other capturing the wake from the central wing and body.

The velocity field in a plane perpendicular to the free-stream flow in the wake behind the bird was measured using a PIV system recording 640 frame-pairs s^{-1} . Two LaVision Imager pro HS4M high-speed cameras (2016×2016 pixels, LaVision, Goettingen, Germany) in stereo configuration were aimed at the left wing tip vortex and an additional two cameras were aimed at the inner wing and body wake region. The combined resolved flow field had a width of 0.45 m and a height of 0.35 m. A 527 nm diode-pumped LDY304PIV laser (Litron Lasers, Rugby, UK) was used to illuminate particles ($\sim 1 \mu m$) in a sheet, approximately 3 mm thick in the streamwise direction, aligned with the plane of focus of the cameras.

The posture of the bird was captured using two LaVision HighSpeedStar3 high-speed cameras (1024×1024 pixels) in stereo configuration looking down on the bird from the top of the test section (Fig. 1B). The cameras were calibrated with a moving checkerboard pattern using routines from the MATLAB Computer Vision Toolbox (The MathWorks, Natick, MA, USA).

Study species

Gliding flight is frequently used by relatively larger birds (Hedenström, 1993). Jackdaws are among the smaller species that extensively use gliding flight in the wild, which makes them suitable for this experiment considering the size limitations of the test section of the wind tunnel. A young jackdaw was taken from a nest near Revingehed, Skåne, Sweden, around the time of fledging (11 June 2013). The bird was kept in an indoor aviary measuring 1.5×1.5×2 m. Food (primarily dried cat food and oats) and water (drinking and bathing) were made available *ad libitum*. Food and bathing water were removed 1 h before training or experiments, to keep the bird motivated and to prevent it from becoming soaked. The bird was trained, using positive reinforcement (audible cues followed by a food reward), to return to the experimenter's hand, to stand on a weighing scale and to keep position when flying in the wind tunnel. It was introduced to the wind tunnel 1 week after capture. The bird reached its final mass within 2 weeks of capture. Because of technical issues, the first usable experiments were recorded on 20 August 2013.

Following the procedure described by Pennycuik (2008), maximum wingspan was measured from the bird in the hand as $b_w = 0.67$ m and wing area was determined from a tracing as $S_w = 0.0652$ m². During the experiments the mass of the bird was measured before and after each session, ranging from 0.211 to 0.221 kg and averaging 0.215 kg.

Experiments were carried out under permission M 33-13 from the Malmö–Lund Animal Ethics Committee.

Posture reconstruction

At each tilt angle (except at 5.0 deg) a calibration was computed following the stereo calibration tool of the MATLAB Computer Vision Toolbox. The cameras were positioned above the bird, where camera 1 was approximately perpendicular to the streamwise–spanwise plane. Reconstructed points had an estimated reconstruction error in the plane of camera 1 of less than 0.5 mm and approximately 2 mm in the out-of-plane direction. For the glide angle of 5.0 deg, no calibration was available, so the calibration at 5.5 deg, which was most similar, was used. Because of the rotation of the wind tunnel, camera 2 had moved a small amount between 5.0 and 5.5 deg. As a result, the estimated reconstruction errors at the glide angle of 5.0 deg were an order of magnitude larger: ~ 1 mm in plane and 12 mm out of plane. In each view, several key points were digitized (see Fig. S2): the tip of the primary feathers (1–10), the tip

of the secondary feathers (11–18), tertials contour (19–20), tip of the rectrices (tail feathers) (21–26), body centre line (27–28), the shoulder joint (29) and the wrist joint (30). Points 19, 20 and 27–30 are not physical marks consistent over all sequences. Instead, variable consistent marks are identified within each sequence. Point 27 (neck) is located at the collar at the transition between fine feathers on the head and the larger body contour feathers. The feathers on the head meet at the centre line of the head, resulting in temporary natural markers that can be identified in both views throughout several frames. Point 28 (rump) is horizontally aligned between the two central rectrices, and its streamwise location was determined similar to point 27.

The reconstructed points were mirrored in the vertical plane through the body centre line 27–28, and the result was visually checked for errors. Wingspan (b'_w) was determined from the maximum distances between any primary feather point to its respective mirrored point. Wing area (S'_w) was computed as the enclosed area between points 1 to 18, 29 and 30 and their mirrored points. Tail span (b'_t) was determined analogous to wingspan using the rectrix points instead. For the tail area (S'_t), an additional point was required, which was positioned one-third of the distance from the rump to neck (approximately the extension of the outboard tail feather to the body centre line). The body angle was determined from the x (streamwise) and z (vertical) coordinates of points 27 and 28. Spanwise camber (η_w) was calculated as the height of a circular arc segment through the y and z coordinates of points 1–6 and 11–16 and their mirrored points. The coordinates were first normalized to the in-flight wingspan and centred. Through non-linear least squares, a circle with radius R and vertical centre z_c was fitted to these points: $z(y) = \sqrt{R^2 - y^2} + z_c$. The spanwise camber was then calculated as the height of the segment:

$$\eta_w = R - \sqrt{R^2 - \frac{1}{4}}. \quad (7)$$

Note that η_w indicates the height as a fraction of the in-flight wingspan. Only fitted curves with $r^2 > 0.9$ were used, as lower quality fitted curves differed considerably from the reconstructed wing shape. Primary separation was determined as the distance (still in the normalized and centred coordinates) of primary 8 away from the arc segment, i.e. as:

$$\eta_p = \sqrt{y_p^2 + (z_p + z_c)^2} - R. \quad (8)$$

Vertical tail gap was determined from the vertical difference between the mean location of points 11–18 (secondaries) and that of points 21–26 (rectrices).

Wake analysis

The wake velocity fields were computed in LaVision Davis 8.1 using a weighted sliding sum of correlation routine [± 2 frames; multipass 64×64 pixels, 50% overlap 2× to 16×16 pixels, 50% overlap; delete correlation value < 0.6 ; 1× strongly remove ($> 2 \times \text{RMS}$), iteratively insert ($< 3 \times \text{RMS}$)]. This routine was chosen to compensate the low correlations due to particle loss (because the largest particle displacement occurs in the smallest dimension of the laser sheet). The raw vector fields were then further processed in MATLAB. At each speed, each view showed a small but distinct false pattern in the background flow in the streamwise direction, most likely because of the relatively high velocity perpendicular to the measurement plane. This pattern was removed by constructing an average second-order surface polynomial, for

each combination of speed and glide angle, that was subtracted from the measured flow and replaced with a uniform streamwise velocity based on the mean velocity from the polynomial. The two views were then merged using weighted averaging favouring vectors with lower temporal signal noise. From the merged velocity field sequence, segments of 40 to 60 frames (63–94 ms) were selected, during which the wake did not notably displace or change shape. For these segments, the time-averaged velocity field $\bar{\mathbf{u}}$ and the root-mean-squared time fluctuations \mathbf{u}' were computed. As only the wake from the left wing and the body wake were captured, a symmetry plane was defined manually, depending on the available information in the wake, to best estimate the location of the right wing tip vortex (see Fig. 2).

Aerodynamic forces on an object immersed in a flow can be computed using a control volume approach (Noca et al., 1999; van Oudheusden et al., 2006). Using such an approach, lift was computed using the wake velocity field equation:

$$L = \rho \iint y \bar{\omega} dS + \rho \iint y \left\{ \bar{w} \frac{\partial \bar{u}}{\partial y} + \bar{v} \frac{\partial \bar{u}}{\partial z} \right\} dS, \quad (9)$$

where $\bar{\omega}$ is the streamwise vorticity (van Dam et al., 1993). Induced drag was computed as:

$$D_{\text{ind}} = \frac{1}{2} \rho \iint \psi \bar{\omega} dS + \frac{1}{2} \rho \iint (v'^2 + w'^2) dS, \quad (10)$$

where ψ is the cross-flow stream function solved from $\nabla^2 \psi = -\bar{\omega}$ with Dirichlet boundary conditions $\psi=0$ on the wind tunnel walls [using the function `adaptmesh()` from the MATLAB Partial Differential Equation Toolbox]. Body drag was computed as:

$$D_{\text{body}} = \rho \iint_{\text{body}} (\bar{u}(U_{\infty} - \bar{u})) dS - \rho \iint_{\text{body}} u'^2 dS, \quad (11)$$

where the body region was defined manually for every wake based on the pattern of the streamwise velocity perturbation (see Fig. 2). Profile drag of the tail is included in this body drag term, even when the tail was widely spread. Wing profile drag was computed using:

$$D_{\text{pro}} = \iint_{\text{pro}} (\bar{u}(U_{\infty} - \bar{u})) dS - \rho \iint_{\text{pro}} u'^2 dS, \quad (12)$$

where the profile drag region was manually masked to include only the velocity deficit due to the wings and to minimize the influence of noise outside of the actual wake (see Fig. 2). Eqns 10 to 12 are derived through a control volume approach (e.g. Giles and Cummings, 1999; van Dam, 1999), where Eqn 10 is the result in the case of only induced drag, and Eqns 11 and 12 result in cases of only profile drag or body drag, respectively.

Eqn 10 only takes into account the affected airstream within the boundaries of the wind tunnel walls. For a bird the size of the jackdaw, this results in a reduction in induced drag of 10–15% compared with what the same distribution of vorticity would produce in an unbounded flow. Shape-specific span efficiency e' was corrected for this wall effect by:

$$e' = \left(\frac{\beta^2}{e} + \sigma \right)^{-1}, \quad (13)$$

where σ depends on the ratio of wingspan to wind tunnel width and the vertical position in the tunnel. Details on this correction can be found in Fig. S1. Effects of wake blockage and solid blockage were found to be negligible: $(\Delta u/U_{\infty})_{\text{wb}} \ll 1\%$ (Barlow et al., 1999, p. 374).

Weight support and effective glide angle

For perfect steady gliding flight, the total aerodynamic force should balance the weight of the bird. In that case, the weight support is equal to $\sqrt{L^2 + D^2}/W=1$. If the measured values deviate from unity, this could indicate that something is wrong with the measurement or that the bird is not perfectly balanced, or a combination of both. From our processed dataset, we discarded measurements that deviated more than 20% from proper weight support. The remaining dataset ($N=389$) had an average weight support of 1.04 with a standard deviation of 0.07. Fig. 3A shows the weight support averaged per combination of glide angle and speed.

The drag component is an order of magnitude smaller than the weight. The required drag for steady gliding flight is $D=W \sin \gamma$. The measured drag increased with decreasing glide angles from an average of 1.08 at 6 deg to 1.28 times the required drag at 4.5 deg (see also Fig. 3B). This trend can be explained simply by considering that at the shallowest glide angle, the required drag matches the minimum drag the bird can produce. Any variation will then increase the average measured drag above that required for a steady glide. This is visualized in Fig. 3C. The bird in practice seems to experience the same variation of drag at the instance of measurement irrespective of the prescribed glide angle. Any measurements should be only weakly related to the wind tunnel angle, on the one hand because of the bird's intention to glide steadily, and on the other hand because of the degree of unsteady aerodynamics involved. We therefore constructed an alternative (quasi-steady) glide angle based on the measured combinations of lift and drag. For visualization purposes we grouped these to the closest half-degree. This left the angles 5.0, 5.5, 6.0 and 6.5 deg, the latter also containing all angles larger than 6.5 deg. Regressions were performed on the complete dataset.

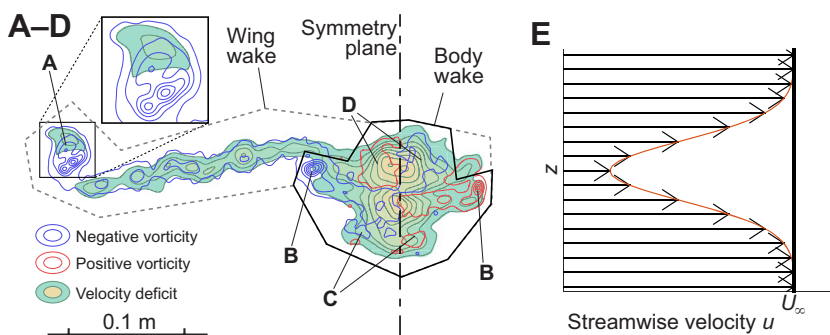


Fig. 2. Visualisation of wake vorticity and velocity deficit at 7.6 m s⁻¹. (A) Wing tip vortex, showing multiple vortex cores. Vorticity is shed along the entire wingspan. (B) Tail tip vortex. Vorticity is found along the entire span of the tail. The tail is contributing positive lift. (C) Lower vortex pair of body quadrupole of lower strength than upper vortex pair (D). Filled contours indicate streamwise velocity deficit. Also indicated are the symmetry plane, the selected region enclosing the body drag and that enclosing the wing profile drag. (E) Schematic representation of the velocity deficit, observed as a vertical slice through the measurement plane. The thick line indicates the free-stream velocity.

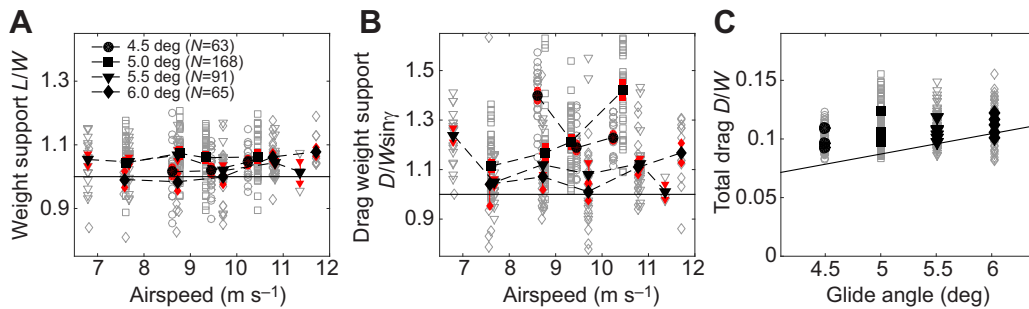


Fig. 3. Weight support and drag weight support for the different combinations of glide angle and airspeed. Grey unfilled markers indicate raw data points. Black filled markers indicate means within groups of 1 m s^{-1} bins and 1 deg bins for glide angles, with the smaller (red) filled markers indicating the corresponding standard errors. Dashed lines connect the means within glide angle group. This applies to all subsequent figures. (A) Average total weight support is close to one. Solid line indicates proper weight support. (B) Average drag weight support increases with reducing tilt angles. Solid line indicates proper weight support. (C) Total drag over weight ($D/W = \sin \gamma$) against the wind tunnel tilt angle. Solid line indicates proper weight support.

Statistics and data availability

In total, 414 wakes were analysed, of which 389 were within 20% of weight support. The posture was analysed for 118 of these wakes. All regressions were performed using the `fitlm()` function of the MATLAB Statistics Toolbox, with response and predictor variables as continuous variables. Summary tables for regressions between aerodynamic components and measures of posture, and the complete dataset are made available as the supplementary material (Tables S1–S6).

RESULTS

Wake topology

Fig. 2 shows a typical wake as captured behind the gliding jackdaw. We measured the wake at a distance of approximately one-half to one full wingspan behind the bird. The vorticity that is shed from the wings has had little time to roll-up into the tip vortices, so that we can still see regions of vorticity distributed along the span. In most conditions, the tail is contributing some positive lift, so that we can also identify a vorticity distribution coming from the tail. Profile drag causes a thin region of decelerated flow leaving the wing. When the tail is spread, a similar region of decelerated flow can be identified for the tail, though only where the tail extends beyond the wake of the body. Behind the body a wider region of decelerated flow is visible. The deceleration in this region is much more substantial than for the wake of the wing. The body region often also contains four patches of vorticity organized as a quadrupole, where the top pair is separated from the lower pair by the tail. The lower pair has the same sign as the tail, i.e. reflecting positive lift, and often merges with tail vorticity. The top pair rotates in opposite sense. Because of the minimal distance from the spanwise centre, these vortices will not actually contribute significantly to the lift; however, their kinetic energy contributes to the measure of the induced drag.

Posture

Wingspan decreases substantially with speed from just over 90% of the maximum wingspan at the lowest speeds to approximately 75% at the higher speeds. However, we find no significant relationship with glide angle ($P_U < 10^{-31}$, $P_\gamma = 0.53$, $N = 118$, $r^2 = 0.68$; the notation P_U and P_γ indicating the P -values for the correlations with U and γ , respectively). Wing area is strongly linked to wingspan, so that wing area shows a very similar pattern (Fig. 4B). In fact, the area ratio $\zeta = S'_w/S_w$ is almost linearly proportional to the span ratio $\beta = b'_w/b_w$ (Fig. 4C). A linear regression, $\zeta = c_0 + c_1\beta$, gives $c_0 = -0.33 \pm 0.04$ and $c_1 = 1.44 \pm 0.04$ (means \pm s.e.m., $N = 118$).

Tail span varied from 28% of the maximum wingspan at the lowest speed to 7% at the highest speed (Fig. 5A). Here we do find a significant positive relationship with glide angle ($P_U < 10^{-49}$, $P_\gamma < 0.001$, $N = 116$, $r^2 = 0.86$). As the tail of a jackdaw has a simple fan shape, its area follows the trend of the tail span (Fig. 5B).

Body angle was measured based on two soft markers on the bird's body, and the camera setup is most sensitive to errors in the vertical direction, so these body angle measurements should be interpreted with caution. However, body drag is likely to be a function of body angle and therefore it is an important parameter to consider. For the equivalent glide angles of 5.0 and 5.5 deg, a decreasing trend is observed, going from 15 deg to approximately 7.0 deg (Fig. 6). The decrease is less apparent for the steeper angles of 6.0 deg and above. A linear model finds a negative relationship with speed, but none with glide angle ($P_U = 0.002$, $P_\gamma = 0.44$, $N = 118$, $r^2 = 0.09$).

More subtle measures of posture include the non-planar features of the wing, which have been suggested as adaptations to minimize induced drag. The most typical for gliding jackdaws is the spanwise camber, where the outer wing is lowered below the wing root. This shape can be approximated as a circular arc segment, of which the span-specific height η_w is shown in Fig. 7A. There does not seem to be a clear relationship between spanwise camber and glide

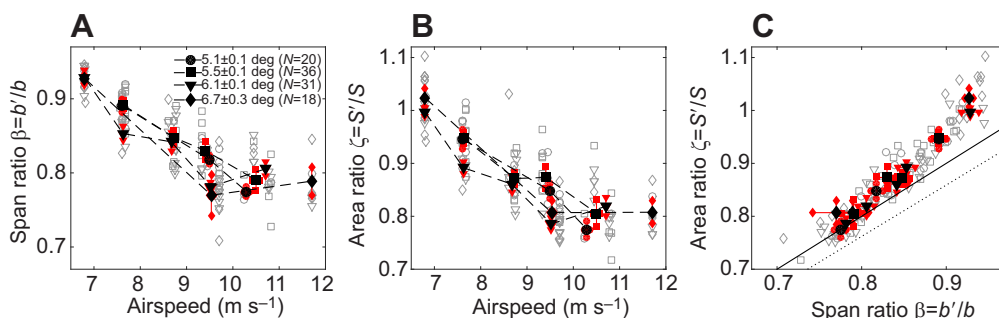


Fig. 4. Wingspan and wing area decrease with speed and are approximately proportional to each other. (A) Wing span ratio as a function of speed averaged for binned equivalent glide angles. (B) Wing area ratio against speed. (C) Wing area ratio against wing span ratio. Solid line indicates 1:1 relationship. Dotted line indicates regression from Rosén and Hedenström (2001). See legend to Fig. 3 for marker descriptions.

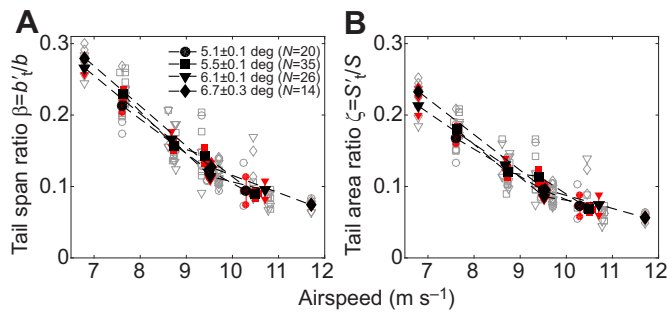


Fig. 5. Tail span and tail area decrease with speed. (A) Tail span relative to the maximum wingspan. Maximum tail span is just over 25% of the maximum wingspan while the minimum is around 10%. (B) Tail area relative to maximum wing area. Maximum tail area is just over 20% of the maximum wing area. See legend to Fig. 3 for marker descriptions.

angle, but there is some tendency for it to increase with speed ($P_U < 10^{-5}$, $P_V = 0.35$, $N = 96$, $r^2 = 0.21$). Separation of the outer primaries, η_p , also increases slightly with speed (Fig. 7B). Below 10 m s^{-1} , the separation is more pronounced for the higher drag cases ($P_U < 10^{-5}$, $P_V < 0.007$, $N = 71$, $r^2 = 0.32$). As shown in Fig. 7C, the tail gap η_t varies non-linearly with speed. Below 9 m s^{-1} , the tail gap is relatively constant with speed and glide angle, averaging 0.054 ± 0.002 ($N = 59$). Above 9 m s^{-1} , η_t varies both with speed and glide angle, where tail gap is reduced at increasing speed, and a larger tail gap is related to increased total drag ($P_U < 10^{-4}$, $P_V = 0.003$, $N = 57$).

Components of drag

Span efficiency decreased with flight speed from approximately 1 to 0.7 (Fig. 8A), and it was generally lower for higher total drag ($P_U < 10^{-51}$, $P_V < 10^{-7}$, $N = 389$, $r^2 = 0.51$). This corresponds to a large extent with the observed span reduction (Fig. 4A). If we remove the effect of wingspan and look at the shape-specific span efficiency e' , most of the variation has disappeared (Fig. 8B), with all values being relatively close to 1. With increasing speed there is a weak increase in e' , while there is a strong relationship between decreased span efficiency and higher total drag ($P_U = 0.008$, $P_V < 10^{-5}$, $N = 118$, $r^2 = 0.21$).

Shape-specific span efficiency can be influenced by non-planar features of the lifting surfaces: spanwise camber η_w , primary separation η_p , tail span β_t/β and vertical tail gap η_t . In a linear model including all four variables, only tail span and tail gap have

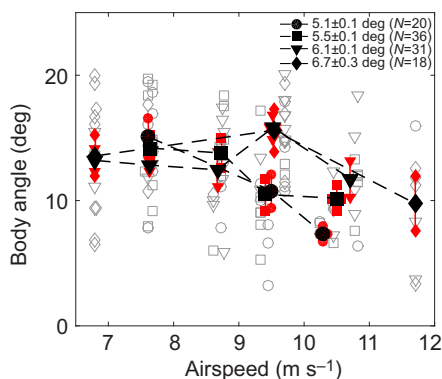


Fig. 6. Body angle for different combinations of glide angle and airspeed. Body angle, measured as the angle between the line from the neck (point 27) to the rump (point 28). See legend to Fig. 3 for marker descriptions.

significant effects ($P_{\eta_w} = 0.31$, $P_{\eta_p} = 0.13$, $P_{\beta_t} = 0.048$, $P_{\eta_t} < 0.001$, $N = 94$), where notably an increase of tail gap of $0.01b'_w$ corresponds to a decrease in span efficiency of approximately 1–2% (see also Table S1). Despite the much lower confidence, spanwise camber, primary separation and tail span are attributed positive contributions to span efficiency.

The profile drag coefficient (Fig. 9A) decreased slightly with flight speed and was lower for smaller glide angles ($P_U < 10^{-4}$, $P_V < 10^{-25}$, $N = 387$, $r^2 = 0.26$). Taking into account the in-flight wing area reduces the dependency on speed (Fig. 9B), but otherwise the effect is marginal. Fig. 9C shows the profile drag coefficient as a function of lift coefficient. Performing a linear regression $C'_{D_{\text{pro}}} = c_0 + c_1 C'_L + c_2 C'^2_L$ (Eqn 4) on the data, we find $k_{\text{pro}} = 0.030$, $C'_{L_{D_{\text{pro,min}}}} = 0.77$ and $C_{D_{\text{pro,min}}} = 0.019$ (using $C'_{D_{\text{pro,min}}} = c_0 - c_1^2/4c_2$ and $C'_{L_{D_{\text{pro,min}}}} = -c_1/2c_2$; see also Table S2). When we include parameters of wing shape, η_w and η_p , in the above regression model, we find that spanwise camber η_w may be affecting both c_0 ($P_{\eta_w} = 0.004$) and c_1 ($P_{\eta_w/C_L} = 0.014$; see also Table S3). This primarily has the effect of lowering the lift coefficient for minimum profile drag, and secondarily, within the observed range for spanwise camber, of lowering the minimum profile drag. The effect of primary separation is uncertain ($P_{\eta_p} = 0.16$; see also Table S3), but may be to increase profile drag.

The body drag coefficient decreases strongly with speed (-0.056 ± 0.002 per m s^{-1}) and there is a clear relationship with glide angle (0.092 ± 0.003 per degree) (Fig. 10A). Theoretically, we may expect body drag to vary with the cube of the body angle (Hoerner, 1965): $\Delta C_{D_b} = \sqrt{4l_b^2/\pi S_b} C_{D_c} |\sin^3 \alpha_b|$. If we add this relationship, with a body length estimate of $l_b = 0.3 \text{ m}$ and a cross-sectional drag coefficient of $C_{D_c} = 1$, to a baseline $C_{D_b} = 0.2$ in Fig. 10B, it lines up with the lower values of body drag coefficient with respect to body angle. However, this pattern explains little of the observed variation in body drag coefficient ($r^2 = 0.06$; see also Table S4). As tail profile drag is included in the measurement of body drag, we may expect the body drag coefficient to vary with tail area, as shown in Fig. 10C. If pressure drag is negligible (Thomas, 1993), the increase in body drag coefficient due to tail profile drag will be almost proportional to the tail area: $\Delta C_{D_{b,t}} = C_{D_{\text{pro,t}}} S'_t/S_b$. Including tail area in the model removes any significance of the body angle, and an estimated correlation coefficient with S'_t/S_b of 0.11 ± 0.01 is found ($r^2 = 0.58$; see also Table S5). However, this is roughly an order of magnitude more than expected for the friction drag coefficient $C_{D_f} = 2.66/\sqrt{Re_t}$, where Re_t is the mean chord Reynolds number of the tail. This suggests that tail pressure drag is not negligible. If we assume that the tail lift coefficient is proportional to the tail area, we would instead expect a cubic scaling with tail area: $\Delta C_{D_{b,t}} \propto (S'_t/S_b)^3$. This results in a coefficient of 0.0093 ± 0.0009 (see also Table S5). If we assume $C_{L_{t,\text{max}}} \approx 1$ corresponds to $(S'_t/S_b)_{\text{max}} \approx 3$, this would correspond to a value of $k_{\text{pro,t}} \approx 0.08$ (i.e. $C_{D_{b,t}} = k_{\text{pro,t}} C'^2_{L_t}$), which is reasonable for low-aspect-ratio wings at Reynolds numbers between 30×10^3 and 60×10^3 (Spedding and McArthur, 2010), such as the tail under consideration.

DISCUSSION

Progress in quantitative wake analysis

In this study we computed induced drag, wing profile drag and body drag from the wake velocity measurements taken from a jackdaw gliding in a wind tunnel. For this we used a method for determining induced drag that is new to animal flight studies. Wake velocity data

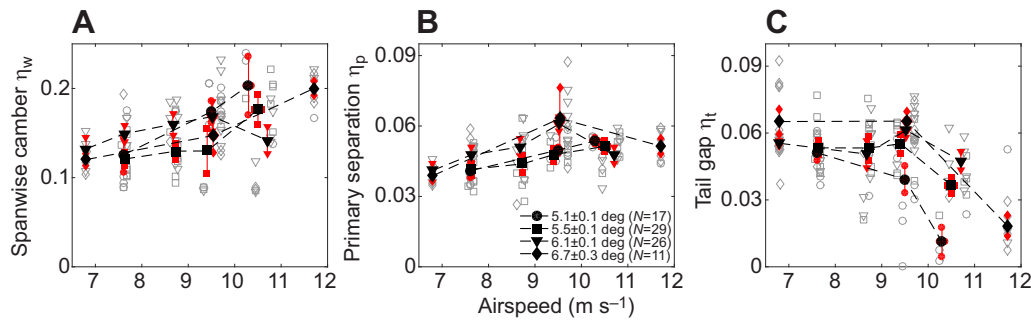


Fig. 7. Measures of non-planar features for different combinations of equivalent glide angle and airspeed. (A) Spanwise camber, the relative height of the circle arc segment fitted through the trailing edge feathers. (B) Primary separation (primary 8), the distance away from the fitted circle arc segment. (C) Vertical tail gap between the trailing edge of the tail and that of the secondary feathers. See legend to Fig. 3 for marker descriptions.

have previously been used to estimate aerodynamic forces in flying animals (e.g. Bomphrey, 2006; Henningsson and Hedenström, 2011; Muijres et al., 2011; Spedding, 1987), but in these studies, simplified wake models were used. In an experiment with a kestrel (*Falco tinnunculus*) gliding through a cloud of helium-filled soap bubbles, the circulation in the trailing wing tip vortex could be estimated, from which the approximate lift force could be computed (Spedding, 1987). A similar approach for estimating lift was used in later studies. Body drag was measured using an approach similar to Eqn 11 for a common swift (*Apus apus*) by Henningsson and Hedenström (2011). However, neither profile drag nor induced drag was measured, so they assumed a span efficiency and then subtracted (measured) body drag and (estimated) induced drag from the total drag to obtain wing profile drag. Recently, induced drag has been estimated in terms of the down-wash distribution in the wake using a form of lifting line model (Bomphrey et al., 2006; Henningsson et al., 2014; Muijres et al., 2011). However, these models rely on the assumption that the wake maintains the shape of the lifting line as it leaves the wing, an assumption that is violated by the rapid formation of trailing tip vortices. Instead, Eqn 10 essentially measures the kinetic energy related to the trailing vorticity, a quantity that persists far downstream of the wing irrespective of wake deformation, making this the most robust approach for measuring induced drag.

Control of drag

All three drag components were involved in controlling the total drag. We related variation in the measured drag components to posture adjustments by the bird. Span reduction and the use of the tail appeared to be the primary variables affecting induced drag. Tail use also has considerable consequences for the body drag. The

profile drag coefficient showed large variation, but we could only attribute a small portion of this variation to any of the measures of posture.

Induced drag

The separation of the outer primary feathers is often mentioned as an adaptation that improves the (shape-specific) span efficiency (Cone, 1962; Eder et al., 2015; Kroo, 2001; Tucker, 1995). However, in our results we did not find such a relationship. Also, the degree of spanwise camber did not appear to have any noticeable effect on span efficiency. Instead, we could only relate the vertical gap between the tail and main wing to span efficiency, where it appears that using the tail has a negative effect on the span efficiency. This seems counterintuitive in the light of Prandtl's biplane model, which states that two vertically separated lifting surfaces can improve span efficiency (Thomas, 1996). This effect is described by the equation:

$$\frac{1}{e'} = 1 - 2(1 - \sigma) \left(\frac{L_t}{W} \right) + \left(1 - 2\sigma + \left(\frac{b'_t}{b'_w} \right)^{-2} \right) \left(\frac{L_t}{W} \right)^2, \quad (14)$$

where the biplane coefficient σ decreases with increasing tail gap. For the jackdaw, the tail to wingspan ratio b'_t/b'_w is <0.03 and the tail gap η_t is <0.05 , corresponding to a σ of >0.08 . This means the tail can only improve span efficiency over the narrow range of tail loadings between 0 and 4% of the total weight. Outside this range, the span efficiency rapidly decreases. This means that a larger tail gap itself will improve span efficiency, but increased tail loading is accomplished by increasing angle of attack, thereby also increasing tail gap.

Considering that the use of the tail has a negative effect, the span efficiency is very close to unity; in fact for minimum tail deployment it is well above unity. As spanwise camber and primary separation were present across all tested conditions, these parameters are still likely to be involved in improving span efficiency, while the limited amount of variation prevents its detection. The span efficiencies we find for this jackdaw are generally much higher than those found for a common swift (Henningsson et al., 2014). As that study used a fundamentally different method, we cannot directly compare these values. However, it is worth noting that common swifts and jackdaws have comparable maximum lift to drag ratios at 12.5 (Henningsson and Hedenström, 2011) and 12.6 (Rosén and Hedenström, 2001), respectively, while the jackdaw has a higher body drag. Additionally, if we consider the Oswald efficiency factor, which combines the span efficiency with the lift-dependent component of

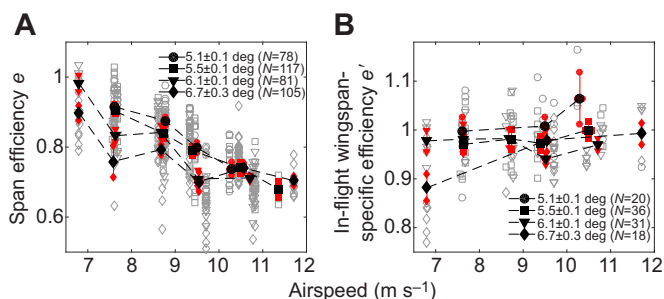


Fig. 8. Variation in span efficiency. (A) Span efficiency using maximum wingspan shows a clear decrease with speed. (B) Span efficiency specific for the in-flight wingspan has much less variation (note vertical axis scale from 0.8 to 1.1). See legend to Fig. 3 for marker descriptions.

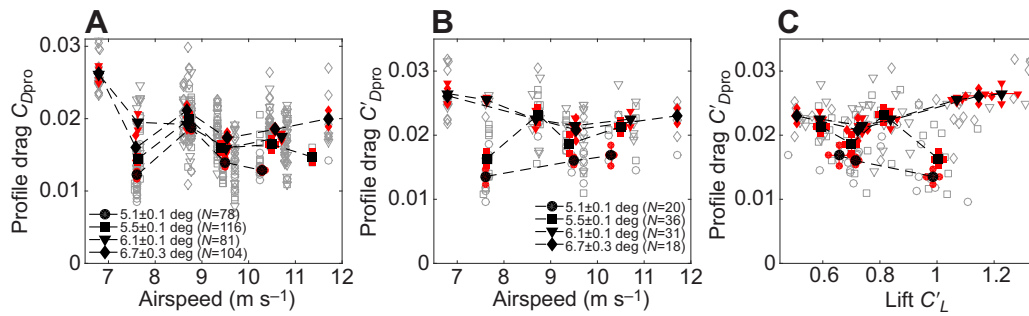


Fig. 9. Variation in the wing profile drag coefficient. (A) Profile drag coefficient relative to maximum wing area as a function of speed. (B) Shape-specific profile drag coefficient (relative to in-flight wing area) as a function of speed. Primarily the right-hand side of the graph is raised compared with A due to the decreased wing area at higher speeds. (C) Shape-specific profile drag coefficient plotted against shape-specific lift coefficient (both based on in-flight wing area). The lower bound, corresponding to the lowest equivalent glide angle, appears to decrease with increasing lift coefficient. See legend to Fig. 3 for marker descriptions.

profile drag, expressed as:

$$e_{\text{Oswald}} = \left(\frac{1}{e} + k_{\text{pro}} A \pi \right)^{-1}, \quad (15)$$

it follows that for large-aspect-ratio wings such as those of common swifts ($A=b^2/S=9.8$), there is less advantage for having a high span efficiency.

Profile drag

For the jackdaw we found profile drag coefficients with a magnitude of approximately 0.02, but with a rather large variation (s.d.=0.005). A previous study measured profile drag of a Harris's hawk (*Parabuteo unicinctus*) using a wake rake to measure stagnation pressure (Pennycuick et al., 1992). They also found profile drag coefficients of approximately 0.02, with a similar large scatter. It was noted that this could have been due to subtle adjustments of the hand wing near the wrist. We found some support that wing shape, particularly the spanwise camber, may play a role in controlling the profile drag. However, the effect of spanwise camber could only explain a small portion of the observed variation (residual s.d.=0.004). A detailed reconstruction of the wing surface around the wrist could possibly resolve this matter at some point. Another reason for large unexplained variation in profile drag could be due to ignoring tail lift. The profile drag coefficient of the main wing would be:

$$C_{Dpro} = C_{D0} + k_{\text{pro}} \left(\hat{C}_L \left(1 - \frac{L_t}{W} \right) - C'_{L_{Dpro,min}} \right)^2, \quad (16)$$

where $\hat{C}_L = W/qS'_w$. However, tail lift should be related to tail span or tail area, and neither seemed to be appreciably correlated to our measures of profile drag. It is possible that the explanation for the large unexplained variation is simply that it represents measurement error. Both profile drag and body drag are calculated as the difference between two large quantities. For the wing profile drag, this difference is particularly small, so that measurement error in the velocity field will have a relatively large influence. As a rough estimate, we could use $\sigma_{C_{Dpro}} \approx (2S_{\text{pro}}/U_{\infty} S_w) \sigma_u$, which is derived from:

$$\sigma_{C_{Dpro}}^2 = \sum \left(\frac{\partial}{\partial u_i} \frac{(u(u - U_{\infty}) \Delta S_{\text{pro}})}{\frac{1}{2} \rho U_{\infty}^2 S_w} \right)^2 \sigma_u^2, \quad (17)$$

assuming that $u/U_{\infty} \ll 1$. In this equation, S_{pro} ($\approx 0.015 \text{ m}^2$) is the area of the wake over which Eqn 12 was evaluated, and σ_u ($\approx 0.1 \text{ m s}^{-1}$) is the random uncertainty on the streamwise component of the measured velocity field. At 10 m s^{-1} , this results in $\sigma_{C_{Dpro}} \approx 0.005$, which is of the same order of magnitude as the residual variation after taking into account the measures of posture.

Body drag

In previous studies, widely varying values for body drag have been found. These were mostly based on mounted frozen bird bodies on a balance in a wind tunnel (e.g. Pennycuick, 1968; Pennycuick et al., 1988; Tucker, 1990). Body drag coefficients varied roughly between 0.2 and 0.4. The validity of these wind tunnel

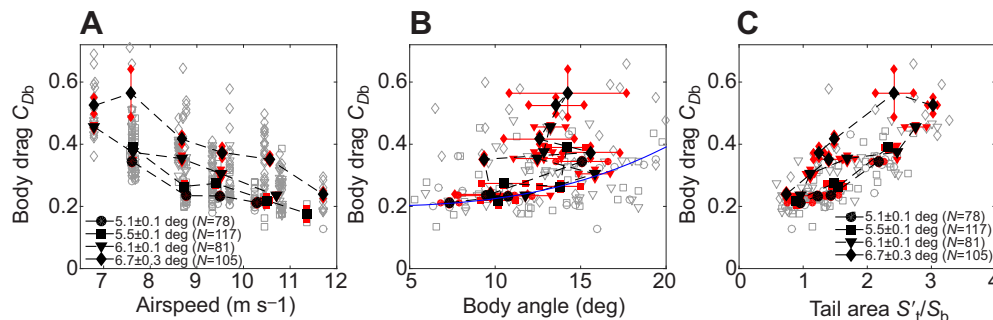


Fig. 10. Variation in the body drag coefficient. (A) Body drag coefficient decreases with speed and is distinctly lower for steeper equivalent glide angles. (B) With respect to body angle, the lower bound of group-averaged body drag coefficients appears to line up with a rough estimate based on an inclined cylinder, indicated by the blue curve. At a body angle of approximately 15 deg, the body drag coefficients diverge upward away from this relationship. (C) Body drag coefficient increases strongly with increasing tail area, indicating the influence of tail profile drag. See legend to Fig. 3 for marker descriptions.

measurements has been questioned (Tucker, 1990), because of both interference drag with the balance mount and possible imperfections in the preening of contour feathers. A smooth model of a peregrine falcon (*Falco peregrinus*) had 40% lower drag than the frozen body it represented, lowering the body drag coefficient to 0.15. Body drag coefficients as low as 0.05 have been proposed (Pennycuick et al., 1996). In a study measuring terminal velocity of small passerines, body drag coefficients ranging from 0.17 to 0.77 were found (Hedenström and Liechti, 2001). However, these coefficients were based on the body frontal area relationship for waterfowl and raptors, $S_b = 0.00813m^{0.666}$ (Pennycuick et al., 1988), whereas for passerines body frontal area is better represented by the relationship $S_b = 0.0129m^{0.614}$ (Hedenström and Rosén, 2003), which makes the lowest estimated body drag coefficient 0.08 and the highest 0.39, with the majority of data points falling between 0.1 and 0.2. For swifts (*Apus apus*), a body drag coefficient was measured varying from 0.3 at the lowest speeds to 0.22 at high speeds, using the same method as in the present study (Henningsson and Hedenström, 2011).

Several studies mentioned above found a negative relationship between speed and body drag coefficient, in the case of mounted frozen bodies clearly independent of body angle or tail use. This was interpreted as a transition through flow regimes (characterized by Reynolds number; Pennycuick et al., 1988). At low Reynolds numbers the flow is less inclined to follow the shape of the body because of a laminar boundary layer, resulting in a large low-pressure area behind the body. In the transitional regime, higher Reynolds numbers promote the transition to turbulent boundary layers, which better resist flow separation. This effect may well have played a role for the jackdaw in the present study. However, the change in body drag coefficient we measured was too dramatic (more than a factor of two) to be fully explained by this phenomenon. Because tail profile drag was included in our measurement of body drag, we think the strong correlation with tail area plays a more dominant role for the jackdaw. For a completely furled tail, the body drag coefficient was approximately 0.2. Few studies have experimentally investigated the effect of the tail on body drag (Johansson and Hedenström, 2009; Maybury and Rayner, 2001). These focused on the function of the tail in the folded condition to potentially act as a splitter plate, reducing the large low-pressure region behind the body. Tail profile drag was included in a bird flight model aimed at studying the function of the avian tail, but only as flat-plate skin friction (Thomas, 1993). However, this friction drag would account for an effect an order of magnitude less than what we observed. Our results indicate that the high body drag coefficient at low speeds is better explained by the pressure component of the tail profile drag.

Finally, it should be noted that bird feet can act as very efficient airbrakes, adding up to 20% to the body drag when lowered completely into the flow (Pennycuick, 1968). Regrettably, we had no cameras recording the position of the feet, so we were unable to relate body drag coefficient to the position of the feet. However, from direct observations it can be said that the legs of the jackdaw were extended to different degrees depending on the flight speed, and at the highest flight speeds they were retracted close to the body. The feet were never tucked under the feathers.

Concluding remarks

Our results show that birds can control aerodynamic drag by using a variety of adjustments in posture. Notably, the use of the tail appears to have a larger effect than often assumed in models used for estimating flight performance in birds, such as the program Flight 1.25 (Pennycuick, 2008).

We also would like to stress the need for caution when using default values for coefficients suggested by said software, as, for example, the default body drag coefficient of 0.1 is half the minimum body drag coefficient we measured for this jackdaw.

Acknowledgements

We thank Johan Nilsson for providing us with the jackdaw. We are also grateful to the members of the Animal Flight Lab at Lund University for their occasional assistance during the experiments and with taking care of the jackdaw.

Competing interests

The authors declare no competing or financial interests.

Author contributions

M.K. and A.H. conceived the study; M.K. and K.W. trained the bird and carried out the experiments; M.K. analysed the data. M.K. drafted the initial draft of manuscript. All authors contributed to the final manuscript.

Funding

The research received funding from the Knut and Alice Wallenberg Foundation (Knut och Alice Wallenbergs Stiftelse) to A.H., an infrastructure grant from Lund University to A.H., the Swedish Research Council (Vetenskapsrådet) to A.H. [621-2009-4965; 621-2012-3585], and the Royal Physiographic Society in Lund (Kungliga Fysiografiska Sällskapet i Lund) to M.K.

Data availability

Raw data will be made available upon request.

Supplementary information

Supplementary information available online at <http://jeb.biologists.org/lookup/suppl/doi:10.1242/jeb.132480/-/DC1>

References

- Barlow, J. B., Rae, W. H. and Pope, A. (1999). *Low-Speed Wind Tunnel Testing*, 3rd edn. New York: Wiley.
- Baudinette, R. V. and Schmidt-Nielsen, K. (1974). Energy cost of gliding flight in herring gulls. *Nature* **248**, 83–84.
- Bomphrey, R. J. (2006). Insects in flight: direct visualization and flow measurements. *Bioinspir. Biomim.* **1**, S1–S9.
- Bomphrey, R. J., Taylor, G. K., Lawson, N. J. and Thomas, A. L. R. (2006). Digital particle image velocimetry measurements of the downwash distribution of a desert locust *Schistocerca gregaria*. *J. R. Soc. Interface* **3**, 311–317.
- Cone, C. D., Jr (1962). The theory of induced lift and minimum induced drag of nonplanar lifting systems. NASA Technical Report R-139. Hampton, VA: NASA Langley Research Center.
- Eder, H., Fiedler, W. and Neuhauser, M. (2015). Evaluation of aerodynamic parameters from infrared laser tracking of free-gliding white storks. *J. Ornithol.* **156**, 667–677.
- Giles, M. B. and Cummings, R. M. (1999). Wake integration for three-dimensional flowfield computations: theoretical development. *J. Aircr.* **36**, 357–365.
- Hedenström, A. (1993). Migration by soaring or flapping flight in birds: the relative importance of energy cost and speed. *Philos. Trans. R. Soc. B Biol. Sci.* **342**, 353–361.
- Hedenström, A. and Liechti, F. (2001). Field estimates of body drag coefficient on the basis of dives in passerine birds. *J. Exp. Biol.* **204**, 1167–1175.
- Hedenström, A. and Rosén, M. (2003). Body frontal area in passerine birds. *J. Avian Biol.* **34**, 159–162.
- Henningsson, P. and Hedenström, A. (2011). Aerodynamics of gliding flight in common swifts. *J. Exp. Biol.* **214**, 382–393.
- Henningsson, P., Hedenström, A. and Bomphrey, R. J. (2014). Efficiency of lift production in flapping and gliding flight of swifts. *PLoS ONE* **9**, e90170.
- Hoerner, S. F. (1965). *Fluid-Dynamic Drag*. Bakersfield, CA: Hoerner Fluid Dynamics.
- Johansson, L. C. and Hedenström, A. (2009). The vortex wake of blackcaps (*Sylvia atricapilla* L.) measured using high-speed digital particle image velocimetry (DPIV). *J. Exp. Biol.* **212**, 3365–3376.
- Kroo, I. M. (2001). Drag due to lift: concepts for prediction. *Annu. Rev. Fluid Mech.* **33**, 587–617.
- Lentink, D., Müller, U. K., Stamhuis, E. J., de Kat, R., van Gestel, W., Veldhuis, L. L. M., Henningsson, P., Hedenström, A., Videler, J. J. and van Leeuwen, J. L. (2007). How swifts control their glide performance with morphing wings. *Nature* **446**, 1082–1085.
- Maybury, W. J. and Rayner, J. M. V. (2001). The avian tail reduces body parasite drag by controlling flow separation and vortex shedding. *Proc. R. Soc. B Biol. Sci.* **268**, 1405–1410.
- Muijres, F. T., Spedding, G. R., Winter, Y. and Hedenström, A. (2011). Actuator disk model and span efficiency of flapping flight in bats based on time-resolved PIV measurements. *Exp. Fluids* **51**, 511–525.

- Noca, F., Shiels, D. and Jeon, D. (1999). A comparison of methods for evaluating time-dependent fluid dynamic forces on bodies, using only velocity fields and their derivatives. *J. Fluids Struct.* **13**, 551–578.
- Pennycuik, C. J. (1968). A wind-tunnel study of gliding flight in the pigeon *Columba livia*. *J. Exp. Biol.* **49**, 509–526.
- Pennycuik, C. J. (1971). Gliding flight of the white-backed vulture *Gyps africanus*. *J. Exp. Biol.* **55**, 13–38.
- Pennycuik, C. J. (2008). *Modelling the Flying Bird*. Amsterdam: Elsevier.
- Pennycuik, C. J., Obrecht, H. H., III and Fuller, M. R. (1988). Empirical estimates of body drag of large waterfowl and raptors. *J. Exp. Biol.* **135**, 253–264.
- Pennycuik, C. J., Heine, C. E., Kirkpatrick, S. J. and Fuller, M. R. (1992). The profile drag of a hawk's wing, measured by wake sampling in a wind tunnel. *J. Exp. Biol.* **165**, 1–19.
- Pennycuik, C. J., Klaassen, M., Kvist, A. and Lindström, Å. (1996). Wingbeat frequency and the body drag anomaly: wind-tunnel observations on a thrush nightingale (*Luscinia luscinia*) and a teal (*Anas crecca*). *J. Exp. Biol.* **199**, 2757–2765.
- Pennycuik, C. J., Alerstam, T. and Hedenström, A. (1997). A new low-turbulence wind tunnel for bird flight experiments at Lund University, Sweden. *J. Exp. Biol.* **200**, 1441–1449.
- Rosén, M. and Hedenström, A. (2001). Gliding flight in a jackdaw: a wind tunnel study. *J. Exp. Biol.* **204**, 1153–1166.
- Spedding, G. R. (1987). The wake of a kestrel (*Falco tinnunculus*) in gliding flight. *J. Exp. Biol.* **127**, 45–57.
- Spedding, G. R. and McArthur, J. (2010). Span efficiencies of wings at low Reynolds numbers. *J. Aircr.* **47**, 120–128.
- Spedding, G. R., Hedenström, A. and Rosén, M. (2003). Quantitative studies of the wakes of freely flying birds in a low-turbulence wind tunnel. *Exp. Fluids* **34**, 291–303.
- Thomas, A. L. R. (1993). On the aerodynamics of birds' tails. *Philos. Trans. R. Soc. B Biol. Sci.* **340**, 361–380.
- Thomas, A. L. R. (1996). Why do birds have tails? The tail as a drag reducing flap, and trim control. *J. Theor. Biol.* **183**, 247–253.
- Tucker, V. A. (1987). Gliding birds: the effect of variable wing span. *J. Exp. Biol.* **133**, 33–58.
- Tucker, V. A. (1990). Body drag, feather drag and interference drag of the mounting strut in a peregrine falcon, *Falco peregrinus*. *J. Exp. Biol.* **149**, 449–468.
- Tucker, V. A. (1993). Gliding birds: reduction of induced drag by wing tip slots between the primary feathers. *J. Exp. Biol.* **180**, 285–310.
- Tucker, V. A. (1995). Drag reduction by wing tip slots in a gliding Harris' hawk, *Parabuteo unicinctus*. *J. Exp. Biol.* **198**, 775–781.
- Tucker, V. A. and Heine, C. E. (1990). Aerodynamics of gliding flight in a Harris' hawk, *Parabuteo unicinctus*. *J. Exp. Biol.* **149**, 469–489.
- Tucker, V. A. and Parrott, G. C. (1970). Aerodynamics of gliding flight in a falcon and other birds. *J. Exp. Biol.* **52**, 345–367.
- van Dam, C. P. (1999). Recent experience with different methods of drag prediction. *Prog. Aerosp. Sci.* **35**, 751–798.
- van Dam, C. P., Nikfetrat, K. and Vijgen, P. M. H. W. (1993). Lift and drag calculations for wings and tails: techniques and applications. In *Fluid Dynamics in Biology* (ed. A. Y. Cheer and C. P. Van Dam), pp. 463–472. Providence, RI: American Mathematical Society.
- van Oudheusden, B. W., Scarano, F. and Casimiri, E. W. F. (2006). Non-intrusive load characterization of an airfoil using PIV. *Exp. Fluids* **40**, 988–992.

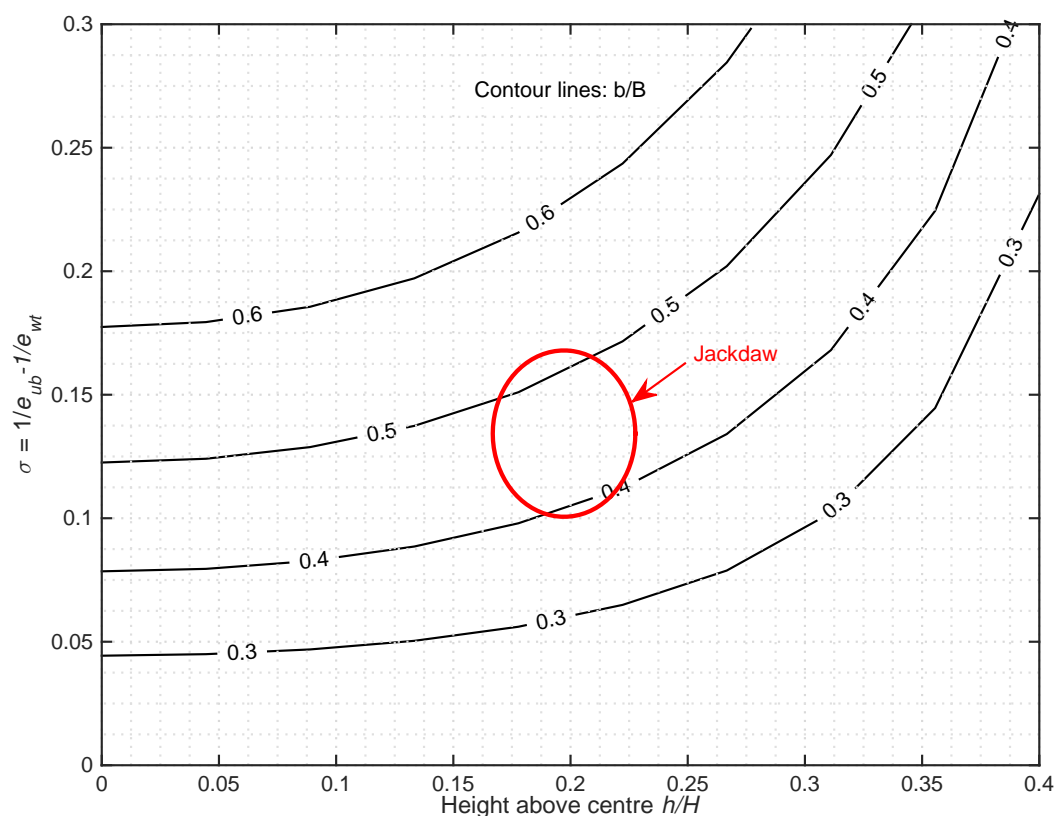


Fig. S1: Induced drag wall correction factor as a function of relative wingspan and height above the wind tunnel centre. Induced drag was calculated by solving the $\nabla^2\psi = -\omega$ over the domain of the wind tunnel cross section. To compute the wall correction for the span efficiency, we used the same procedure for a simulated pair of ideal vortices. We then computed the corrections for a range of vertical positions and wingspans, to which we fitted a cubic interpolation function. For correcting the shape specific span efficiency, we then used the height of the wing tip vortex above the centre of the wind tunnel relative to the height of the wind tunnel, and the inflight wingspan relative to the width of the wind tunnel.

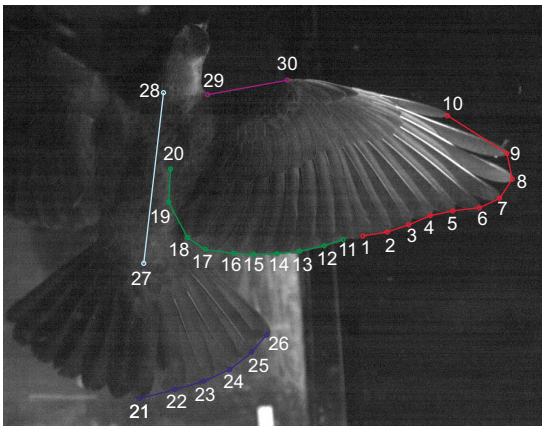


Fig. S 2: Posture reconstruction definitions. Points 1 to 10 primary feather tips; 11 to 20 secondary/tertiary feather tips; 21 to 26 rectrices; 27 rump; 28 neck; 29 shoulder; 30 wrist. Points 27 to 30 are not clearly defined markers. Body centre line appears off in this picture due to perspective and the three dimensional shape of the bird.

Table S 1: Regression shape specific span efficiency. Shape specific span efficiency e' (SpanEfficiency) related to spanwise camber η_w (SpanCamb), primary separation η_p (PrimSep), tail span β_t (TailSpan) and tail gap η_t (TailGap).

Linear regression model:				
SpanEfficiency ~ 1 + SpanCamb + PrimSep + TailGap + TailSpan				
Estimated Coefficients:				
	Estimate	SE	tStat	pValue
(Intercept)	0.944	0.0385	24.5	2.30e-41
SpanCamb	0.173	0.170	1.02	0.311
PrimSep	1.01	0.662	1.52	0.131
TailGap	-1.27	0.337	-3.78	0.000287
TailSpan	0.175	0.0876	2.00	0.0486
Number of observations: 94, Error degrees of freedom: 89				
Root Mean Squared Error: 0.047, R-Squared: 0.251, Adjusted R-Squared 0.217				

Table S2: Regression shape specific profile drag coefficient. Shape specific profile drag coefficient $C'_{D_{pro}}$ (ProfileDrag) related to shape specific lift coefficient C'_L (LiftCoef).

Linear regression model:				
ProfileDrag ~ 1 + LiftCoef + LiftCoef^2				
Estimated Coefficients:				
	Estimate	SE	tStat	pValue
(Intercept)	0.0368	0.00448	8.22	3.47e-13
LiftCoef	-0.0468	0.0118	-3.98	0.000120
LiftCoef^2	0.0304	0.00716	4.25	4.33e-05
Number of observations: 118, Error degrees of freedom: 115				
Root Mean Squared Error: 0.005, R-Squared: 0.150, Adjusted R-Squared 0.135				

Table S3: Regression shape specific profile drag coefficient. Shape specific profile drag coefficient $C'_{D_{\text{pro}}}$ (ProfileDrag) related to shape specific lift coefficient C'_L (LiftCoef), spanwise camber η_w (SpanCamb) and primary separation η_p (PrimSep).

Linear regression model:				
ProfileDrag $\sim 1 + \text{PrimSep} + \text{SpanCamb} * \text{LiftCoef} + \text{LiftCoef}^2$				
Estimated Coefficients:				
	Estimate	SE	tStat	pValue
(Intercept)	0.0579	0.0106	5.47	3.98e-07
SpanCamb	-0.135	0.0452	-2.98	0.00371
PrimSep	0.0832	0.0590	1.41	0.161
LiftCoef	-0.0875	0.0204	-4.30	4.34e-05
SpanCamb:LiftCoef	0.177	0.0706	2.50	0.0142
LiftCoef ²	0.0409	0.00852	4.80	6.16e-06
Number of observations: 96, Error degrees of freedom: 90				
Root Mean Squared Error: 0.004, R-Squared: 0.240, Adjusted R-Squared 0.198				

Table S4: Regression body drag coefficient and body angle. Body drag coefficient C'_{D_b} (BodyDrag) related to expected increase due to body angle $\Delta C_{D_b, \alpha_b} = \sin^3 \alpha_b$ (sin3BodyAng).

Linear regression model:				
BodyDrag $\sim 1 + \sin 3 \text{BodyAng}$				
Estimated Coefficients:				
	Estimate	SE	tStat	pValue
(Intercept)	0.274	0.0158	17.3	5.73e-34
sin3BodyAng	0.555	0.196	2.83	0.00550
Number of observations: 118, Error degrees of freedom: 116				
Root Mean Squared Error: 0.107, R-Squared: 0.065, Adjusted R-Squared 0.056				

Table S5: Regression body drag coefficient and tail area. Body drag coefficient C'_{D_b} (BodyDrag) related to relative tail area S'_t/S_b (TailArea).

Linear regression model:				
BodyDrag $\sim 1 + \sin 3 \text{BodyAng} + \text{TailArea}$				
Estimated Coefficients:				
	Estimate	SE	tStat	pValue
(Intercept)	0.113	0.0173	6.49	2.70e-09
sin3BodyAng	0.214	0.134	1.60	0.113
TailArea	0.109	0.00976	11.2	9.91e-20
Number of observations: 110, Error degrees of freedom: 107				
Root Mean Squared Error: 0.069, R-Squared: 0.577, Adjusted R-Squared 0.569				
Linear regression model:				
BodyDrag $\sim 1 + \sin 3 \text{BodyAng} + \text{TailArea}^3$				
Estimated Coefficients:				
	Estimate	SE	tStat	pValue
(Intercept)	0.228	0.0116	19.6	3.23e-37
sin3BodyAng	0.194	0.139	1.40	0.165
TailArea ³	0.00933	0.000888	10.5	3.61e-18
Number of observations: 110, Error degrees of freedom: 107				
Root Mean Squared Error: 0.071, R-Squared: 0.547, Adjusted R-Squared 0.539				

Table S6. Data set used for the analysis of the gliding flight of a gliding jackdaw. ID: identifier; AirSpeed: wind tunnel air speed (m/s); GlideAngle: tilt angle of the wind tunnel (deg); Weight: recorded total body weight (N); Lift: lift force measured from the wake (N); LiftCoef: lift coefficient based on wing reference area (-); DragWeightSupport: measured drag as fraction of required drag for steady glide based on tilt angle (-); WeightSupport: measured aerodynamic force as fraction of required for steady glide based on tilt angle (-); Dideal: modelled induced drag for elliptically loaded full span wing (N); DragInduced: measured induced drag (N); SpanEfficiency: Dideal/DragInduced (-); DragCoef_ind: induced drag coefficient (-); DragProfile: measured profile drag (N); DragCoef_pro: profile drag coefficient (-); DragBody: measured body drag (N); DragCoef_body: body drag coefficient (-); WingSpan: (m); WingArea: (m²); TailSpan: (m); TailArea: (m²); TailHeight: measured distance between tail trailing edge and main wing trailing edge (m); PrimSep8: distance between primary 8 and main wing arc circle normalized by wingspan (-); BodyAngle: (degrees); SpanRatio: wingspan as fraction of full wingspan (-); SpanCamber: height of the circular arc segment, normalized by wingspan (-); Height: distance above wind tunnel centre (m); EqQuasiSteadyGlideAngle: equivalent glide angle that matches weight support (degrees).

[Click here to Download Table S6](#)